Transmission electron microscopy study on $FeSi_2$ nanoparticles synthesized by electron-beam evaporation

Jong Han Won[a)]
Department of Materials Science and Engineering, Osaka University, Suita, Osaka 565-0871, Japan

Kazuhisa Sato, Manabu Ishimaru, and Yoshihiko Hirotsu
The Institute of Scientific and Industrial Research, Osaka University, Ibaraki, Osaka 567-0047, Japan

(Received 7 March 2006; accepted 21 April 2006; published online 13 July 2006)

We have synthesized epitaxially grown iron disilicide ($FeSi_2$) nanoparticles using an electron-beam evaporation technique and characterized them by transmission electron microscopy (TEM). An Fe film was deposited on a Si(100) substrate, followed by thermal annealing at 1073 K for 2 h. It was found that epitaxially grown nanoparticles with an average size of ~10 nm were formed just beneath the Si surface, suggesting that the deposited Fe atoms diffuse into the substrate. Every single phase of nanoparticles was examined in detail by TEM observation, nanobeam electron diffraction, and energy-dispersive x-ray spectroscopy. Plan-view and cross-sectional TEM observations revealed that these nanoparticles consist of α-, β-, and γ-$FeSi_2$. It was found that the morphology of nanoparticles is closely related to the phases. The α and β phases consist of angled hemisphere and asymmetric triangle-shaped nanoparticles, respectively, while the γ phase consists of hemispherical or columnar-shaped nanoparticles. These particle morphologies are discussed with respect to the lattice mismatches between the particles and the matrix. © *2006 American Institute of Physics*. [DOI: 10.1063/1.2209751]

I. INTRODUCTION

The Fe–Si system is one of the environmental-friendly materials because of their abundant existence on the Earth's crust and no chemical pollution. There exist several compounds in the equilibrium phase diagram of the Fe–Si binary alloy,[1] such as Fe_2Si, Fe_5Si_3, FeSi, and $FeSi_2$. Among these compounds, semiconducting orthorhombic β-$FeSi_2$ has many merits for the industrial applications due to its excellent physical properties such as a direct band gap of 0.8–0.85 eV (Refs. 2–4) and large optical absorption[5] and Seebeck coefficients.[6] In addition, this material can be grown epitaxially on Si(100) and Si(111) substrates.[7,8] Therefore, β-$FeSi_2$ is a promising material that can be used for Si-based optoelectronic devices[9] and photovoltaic material such as solar cell.[10]

Until now, various kinds of growth techniques such as molecular beam epitaxy,[11,12] solid phase epitaxy,[13] reactive deposition epitaxy,[14,15] and ion beam synthesis[16] have been employed to achieve epitaxially grown β-$FeSi_2$ phase on or in a Si substrate. However, the light emitting properties are still highly scattered: some researchers found an effective light emission, while the others reported a weak or no light emission. It was pointed out that the origin of the light emission is attributed to a difference of lattice strains in β-$FeSi_2$.[17–19] The fabrication of well-isolated β-$FeSi_2$ nanoparticles on a Si substrate is one of the possible ways to control the strain state by adjusting the particle size, but only few reports on structural analysis of well-isolated $FeSi_2$ nanoparticles were published.[20–22]

In this study, we employed an electron-beam evaporation technique to fabricate epitaxially grown isolated $FeSi_2$ nanoparticles on a Si(100) substrate, since we have succeeded in forming uniformly distributed metal nanoparticles on a single crystalline substrate using this technique.[23–25] We examined in detail the morphologies of the as-formed $FeSi_2$ nanoparticles and the crystallographic orientation relationships between nanoparticles and substrate using transmission electron microscopy (TEM).

II. EXPERIMENTAL PROCEDURES

Specimens were prepared by an electron-beam evaporation technique using pure Fe (99.97%) and Al_2O_3 (99.99%) crystals as evaporation sources. Si(100) substrates were chemically etched with an etchant $HF:H_2O=1:50$. After eliminating the oxide layer, the substrates were supplied into a vacuum chamber and heated at a temperature of 823 K for 1 h to degas the substrate surface. During the deposition, the substrates were kept at 773 K in a vacuum of 10^{-6} Pa. The thickness of deposited Fe film monitored by a quartz oscillator was 2 nm. An amorphous Al_2O_3 film of 7 nm was further deposited to protect the Fe film from oxidation. Finally, the as-deposited specimens were annealed at 1073 K for 2 h in a vacuum of 10^{-3} Pa using a high frequency induction furnace.

The specimens obtained here were characterized using a JEOL JEM-3000F TEM with an incident electron energy of 300 keV. Plan-view and cross-sectional TEM specimens were prepared using a combination of mechanical polishing and ion thinning with 2.5 keV Ar^+ ions. Nanobeam electron diffraction (NBED), energy-dispersive x-ray spectroscopy with nanoprobe (nano-EDX), and high-resolution TEM (HR-TEM) observations in combination with fast Fourier trans-

[a)]Electronic mail: jhwon22@sanken.osaka-u.ac.jp

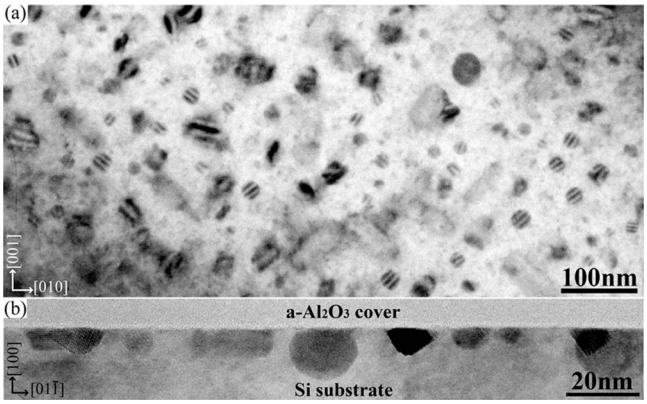

FIG. 1. Bright-field TEM images of the specimen annealed at 1073 K for 2 h. (a) Plan-view image taken at nearly $[100]_{Si}$ pole shows that isolated nanoparticles are dispersed on a Si substrate. (b) Cross-sectional image taken at nearly $[011]_{Si}$ reveals that deposited Fe atoms completely diffuse into Si substrate and form the various shapes of nanoparticles.

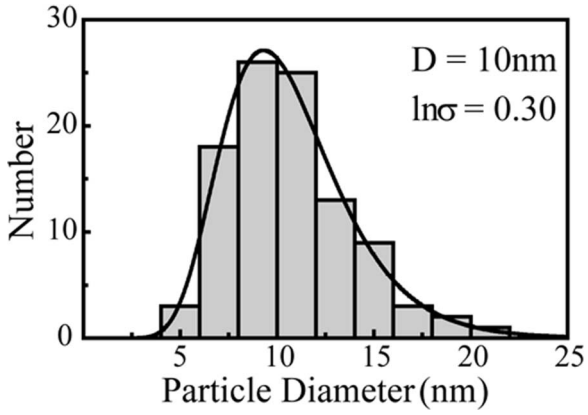

FIG. 2. Mean particle size and distribution. The nanoparticles are uniformly distributed on Si substrate, and their mean size is 10 nm.

form (FFT) analysis were employed to determine the phases of the nanoparticles and the orientation relationships between the nanoparticle and substrate.

III. RESULTS AND DISCUSSION

The formation of cubic ε-FeSi phase was confirmed in as-deposited specimens (not shown), while $FeSi_2$ nanoparticles were obtained after annealing the as-deposited specimens at 1073 K for 2 h. Figure 1 shows an example of (a) plan-view and (b) cross-sectional bright-field TEM images of the annealed specimens. In Fig. 1(a), round-shaped nanoparticles showing moiré fringes are dispersed on a Si(100) substrate. The lattice mismatch between the nanoparticle and Si substrate gives rise to moiré fringes in the nanoparticle images. It should be noted that the moiré fringe spacing and direction largely depend on the particle size and shape. This must be attributed to the formation of different phases and/or the lattice distortion under the strains. On the other hand, cross-sectional TEM observations [Fig. 1(b)] demonstrate that the nanoparticles are formed just beneath the Si surface, suggesting that the deposited Fe atoms diffuse into and react with Si substrate during the annealing process due to the fast diffusion of Fe in Si.[26] The nanoparticles show various kinds of morphologies such as round, triangle, bottom-flat, and columnar shapes. It was presumed that the different morphologies correspond to the different phases and/or crystal orientations.

The size distribution for the nanoparticles estimated from the plan-view observations is indicated in Fig. 2. The particle size was defined as the arithmetical mean of the minor and the major axes of the ellipse, and the total counting number was 100 from the TEM micrograph. The mean particle size is 10 nm with a standard deviation of $1n\sigma=0.30$. The nanoparticles were formed inside the substrate by the diffusion of Fe during postdeposition annealing process, and the size distribution follows a log-normal distribution (solid line) which is often observed in the nanoparticles on the substrate surface formed by evaporation.[27]

Selected-area electron diffraction (SAED) patterns of the annealed specimens are shown in Fig. 3. These SAED patterns were obtained from (a) the [100] (plan-view) and (b) the [011] (cross-sectional) directions of the Si substrate. In addition to strong Bragg reflections of Si, extra spots due to the nanoparticles are apparent in both diffraction patterns. The extra spots show symmetric net patterns, suggesting that there are certain orientation relationships between the nanoparticles and substrate. The SAED patterns were obtained from the region of ~200 nm in diameter, much larger than the size of nanoparticles in plan-view observation: several nanoparticles with different orientations contribute to the formation of Fig. 3(a). On the contrary, the numbers of particles which can be included in selected-area aperture were limited in the cross-sectional image [Fig. 3(b)]. From the analysis of the symmetry and lattice spacings of extra spots, the diffraction patterns of Figs. 3(a) and 3(b) can be explained by the overlap of tetragonal α- and cubic γ-$FeSi_2$ phases. The net

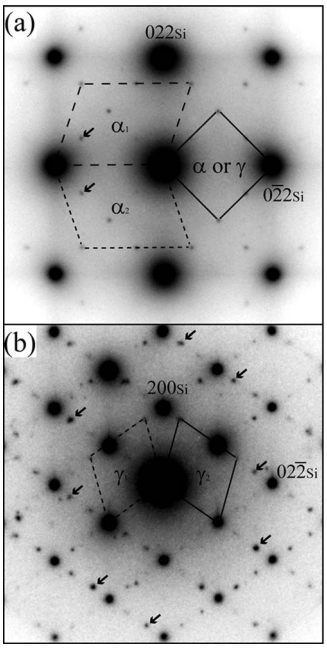

FIG. 3. SAED patterns taken from (a) $[100]_{Si}$ (plan-view) and (b) $[011]_{Si}$ (cross-section) directions. Strong reflections are indexed as Si and extra reflections are due to α- and γ-$FeSi_2$ nanoparticles. The reflections are consistent with $[\bar{2}\bar{1}1]_{\alpha 1}$, $[21\bar{1}]_{\alpha 2}$, $[001]_{\alpha \text{ or } \gamma}$, $[110]_{\gamma 1}$, and $[110]_{\gamma 2}$ net patterns. The arrows indicate double diffraction by Si substrate.

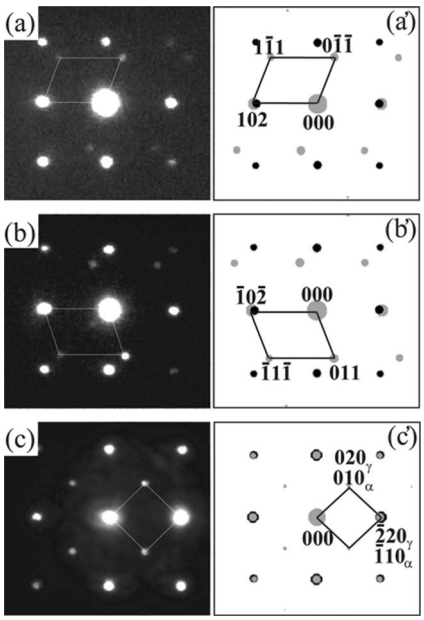

FIG. 4. [(a)–(c)] Nanobeam diffractions and [(a′)–(c′)] simulated patterns along the $[100]_{Si}$ (plan-view) direction of Si substrate. The black and gray spots correspond to Bragg refractions of Si and $FeSi_2$, respectively.

patterns in Fig. 3(a) consist of the variant relations such as $[\bar{2}\bar{1}1]_{\alpha 1}$, $[21\bar{1}]_{\alpha 2}$, and $[001]_{\alpha \text{ or } \gamma}$. On the other hand, two variants of γ_1 and γ_2 were observed in Fig. 3(b) due to the lack of observed nanoparticles and they correspond to beam $\|[110]_\gamma$. Both α- and γ-$FeSi_2$ phases are metastable phases under the present annealing temperature, and they are often observed in nanoparticles.[28–31]

A NBED technique was employed to confirm the validity of the interpretation for the SAED patterns. Figures 4(a)–4(c) show the NBED patterns of the nanoparticles obtained with a probe size of ~10 nm. Simulated diffraction patterns with intensities $|F_{hkl}|^2$corresponding to Figs. 4(a)–4(c) are also displayed in Figs. 4(a′)–(c′). The structure factor, F_{hkl}, where *hkl* represents a specific Bragg reflection, was calculated using $F_{hkl}=\Sigma f_n \exp[2\pi i(hx_n+ky_n+lz_n)]$, where f_n is the atomic scattering factor for atom *n* at a position (x_n, y_n, z_n). The NBED pattern in Fig. 4(a) obviously shows a single crystal $[21\bar{1}]$ pattern from an α-$FeSi_2$ which has a variant with Fig. 4(b) On the other hand, Fig. 4(c) corresponds to the diffraction pattern of [001] α- or [001] γ-$FeSi_2$. It should be noted that the (010) spacing of α -$FeSi_2$ is almost the same as the (020) spacing of γ-$FeSi_2$, and therefore it is difficult to distinguish them in plan-view observations only.

As described above, it was found that the nanoparticles possess a variety of morphologies. To identify the relationships between the crystalline structure and morphology of nanoparticles, HRTEM observations were performed for cross-sectional samples. Figure 5(a) shows an example of the HRTEM image obtained from a hemispherical nanoparticle. The atomic arrangements of the HRTEM image inside the nanoparticle are the same as those of Si substrate. In fact, the FFT pattern of the nanoparticle [the inset of Fig. 5(a)] shows a net pattern similar to the (011) reciprocal plane of Si. To confirm the dissolution of Fe atoms in the particle, nano-

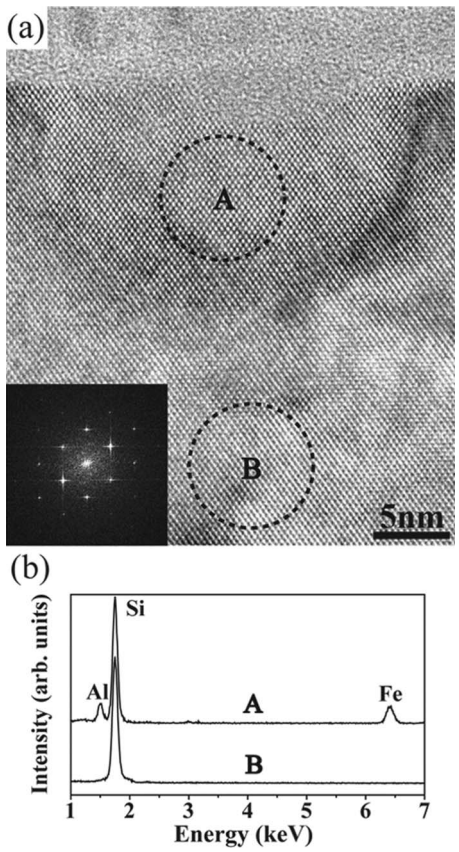

FIG. 5. (a) HRTEM image of γ-$FeSi_2$ nanoparticle with a hemisphere shape, together with its FFT pattern. (b) Nano-EDX spectra obtained from regions A and B in (a).

EDX measurements were performed. Figure 5(b) shows the nano-EDX spectra obtained from regions A and B in Fig. 5(a). The intensities of characteristic x-ray were normalized by those of Si $K\alpha$. In addition to Si $K\alpha$ peak, Fe $K\alpha$ peak is observed in region A, suggesting that the nanoparticle is an Fe–Si compound. The γ-$FeSi_2$ phase is a candidate for this nanoparticle because it has a CaF_2 structure with a nearly identical lattice parameter (a_0=0.5431 nm) to that of Si.[29,30] The orientation relationship between γ-$FeSi_2$ and Si substrate is $(004)_\gamma \| (400)_{Si}$ and $[110]_\gamma \| [011]_{Si}$.

In Fig. 6(a) is shown a nanoparticle with a columnar shape. Nano-EDX measurements revealed the existence of Fe element in the nanoparticle (not shown). The columnar-shaped nanoparticles contain periodic lattice fringes along the $[111]_{Si}$ direction and their spacings are approximately 0.94 nm. From the NBED and FFT patterns in Figs. 6(b) and 6(c), it is found that the nanoparticle has a periodic lattice along the $[111]_{Si}$ direction with a triple period of $(111)_{Si}$. Such a periodic structure was also observed by other researchers, but its atomic model is still controversial. Behar *et al.*[30] and Desimoni *et al.*[31] have explained that the origin of the periodic lattice image is the superimposition of γ-$FeSi_2$ phase and Si, while Shao and Homewood[32] attributed it to a strained β-$FeSi_2$ phase. To identify the structure with the periodic fringes, we carried out HRTEM image simulation using a multislice method.[33] As a consequence, it was concluded that the periodic lattice fringes originate from the superimposition of γ-$FeSi_2$ and Si. Table I shows the numerical

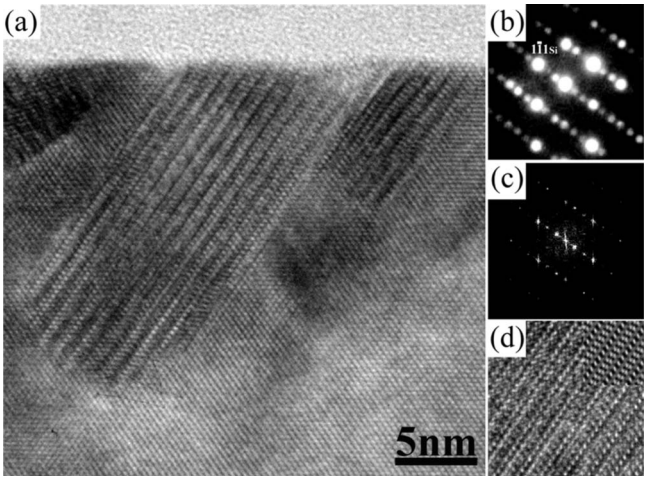

FIG. 6. (a) HRTEM image of nanoparticle with a periodic layered structure. Columnar-shaped nanoparticle is grown along $[111]_{Si}$ and it reveals the periodic fringes with a spacing of ~0.94 nm. (b) NBED pattern and (c) FFT pattern of HRTEM image show that both patterns contain three periodic spots along $[111]_{Si}$. (d) Comparison of the experimental and simulated HRTEM images.

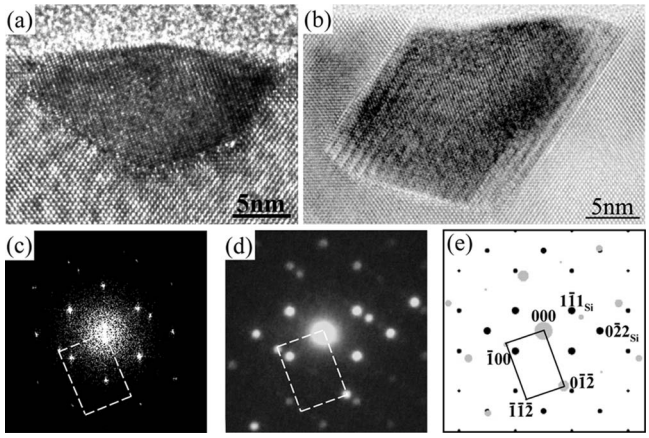

FIG. 7. HRTEM images of α-$FeSi_2$ nanoparticle with (a) angled shape and (b) columnar shape. (c) FFT pattern from the experimental HRTEM image. (d) NBED and (e) simulated patterns with indexing show that the orientation relationship between α-$FeSi_2$ (gray) and Si (black) substrate is as follows: $(\bar{1}12)_\alpha \| (11\bar{1})_{Si}$ and $[0\bar{2}1]_\alpha \| [011]_{Si}$.

parameters used for the multislice calculation. A multilayered supercell was formed by piling γ-$FeSi_2$ up on the Si substrate in which the orientation relationship is $(1\bar{1}1)_\gamma \| (1\bar{1}1)_{Si}$ and $[110]_\gamma \| [011]_{Si}$. The resultant image [the inset of Fig. 6(d)] reproduces the experimental HRTEM image well. It was also confirmed that the fringe images parallel to $(111)_{Si}$ with a period of ~0.94 nm can be interpreted as a moiré fringe. The periodicity of moiré fringe, L, is given as

$$L = \frac{d_1 d_2}{(d_1^2 + d_2^2 - 2d_1 d_2 \cos\phi)^{1/2}},$$

where d_1 and d_2 are the plane distances and ϕ is defined as the rotation angle of those two planes.[34] From the value of $d_{(200)Si}$=0.272 nm, $d_{(111)\gamma}$=0.314 nm, and ϕ=15.8°, L becomes 0.942 nm which is in good agreement with the experimental value.

Figures 7(a) and 7(b) show typical cross-sectional HRTEM images of α-$FeSi_2$ nanoparticles which are one of the dominant phases confirmed by SAED patterns [Fig. 3(a)]. Two different shapes of α-$FeSi_2$ were observed: one is angled hemispherical-like shape with small size [Fig. 7(a)] and the other is columnar shape [Fig. 7(b)]. Both nanoparticles reveal the same FFT and NBED patterns, as shown in Figs. 7(c) and 7(d), respectively. The orientation relationship between α-$FeSi_2$ and Si substrate is always as follows: $(\bar{1}12)_\alpha \| (11\bar{1})_{Si}$ and $[0\bar{2}1]_\alpha \| [011]_{Si}$ [see also Fig. 7(e)]. This orientation relationship is also confirmed from the plan-view direction.

Besides α- and γ-$FeSi_2$ phases, there exist some semiconducting β-$FeSi_2$ nanoparticles even though the thickness of the deposited Fe film is very thin (~2 nm). Figure 8(a) shows a cross-sectional HRTEM image of β-$FeSi_2$ with asymmetric triangle shape and a size of several nanometers. The experimental HRTEM image is well consistent with the simulated multislice image from the zone axis of $[001]_\beta$ [the right corner of the inset in Fig. 8(a)]. Figures 8(b) and 8(c) show that the crystallographic orientation relationship between β-$FeSi_2$ and Si substrate is as follows: $(220)_\beta$ 6.5° from $(1\bar{1}1)_{Si}$ and $[001]_\beta \| [011]_{Si}$. Unlike the cases of α- and γ-$FeSi_2$ nanoparticles, strain contrasts along the silicide and matrix boundary can be seen in Fig. 8(a) as indicated by the arrows. The bright strain contrasts with the small spacing (single arrows) and large spacing (double arrows) originate from the lattice mismatches. To investigate the origin of these contrasts, Fourier filtering analysis was applied. Figure

TABLE I. Numerical parameters for multislice simulations.

Crystal	Si	γ-$FeSi_2$
Structure type	Diamond	CaF_2
Space group	$Fd\bar{3}m$	$Fm\bar{3}m$
Lattice parameter	$a_0=b_0=c_0$=0.5428 nm	$a_0=b_0=c_0$=0.5431 nm
Supercell size (nm) projected to $[110]_\gamma$ and $[011]_{Si}$	a=5.4286 nm, b=7.6772 nm, c=3.8386 nm	a=5.4310 nm, b=7.6806 nm c=3.8403 nm
Zone axis	$[011]_{Si}$	
Epitaxial relationship	$(1\bar{1}1)_\gamma // (1\bar{1}1)_{Si}$ and $[110]_\gamma // [011]_{Si}$	
Slice thickness	0.1 nm	
Accelerating voltage	300 kV	
Spherical aberration (Cs)	0.6 mm	
Defocus (Δf)	350 Å	

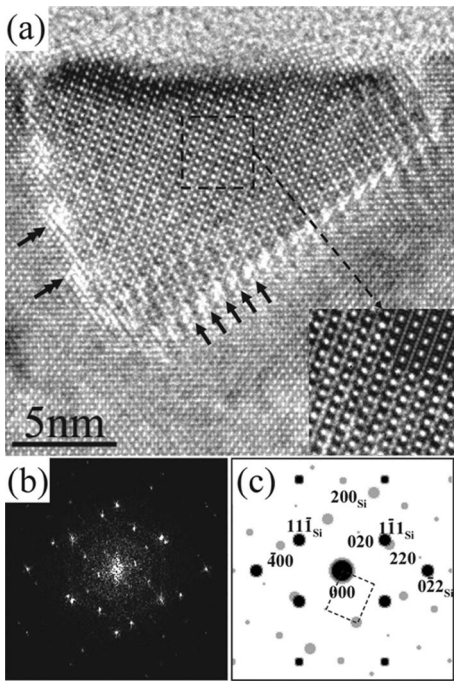

FIG. 8. (a) HRTEM images of β-$FeSi_2$ nanoparticle with asymmetric triangle shape. The simulated image is indicated in the right corner of the inset. The strain contrasts due to lattice mismatch between particle and substrate can be seen as indicated by the arrows. (b) FFT and (c) simulated diffraction patterns with indexing show that the orientation relationship between β-$FeSi_2$ (gray) and Si (black) substrate is as follows: $(220)_\beta$ and $(1\bar{1}1)_{Si}$ have a mismatch angle of 6.5° at the zone axis of $[001]_\beta \| [011]_{Si}$

9(a) shows the Fourier filtered image of the area at the interface between β-$FeSi_2$ and Si, which corresponds to the region with the small-spacing contrasts in Fig. 8(a). This image was extracted from $\bar{4}00_\beta$ and $11\bar{1}_{Si}$ spots in the FFT pattern

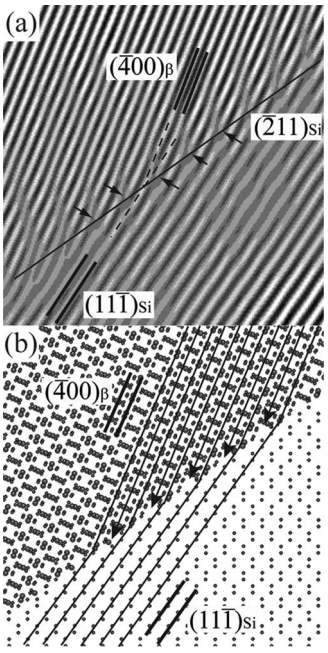

FIG. 9. Fourier filtered image obtained from (a) $\bar{4}00_\beta$ and $11\bar{1}_{Si}$ (small-spacing) spots in Fig. 8(b). The distances of small spacing are consistent with those of HRTEM image in Fig. 8(a). Schematic diagram of (b) shows the dislocation edges at the interfaces of β-$FeSi_2$ and Si matrix.

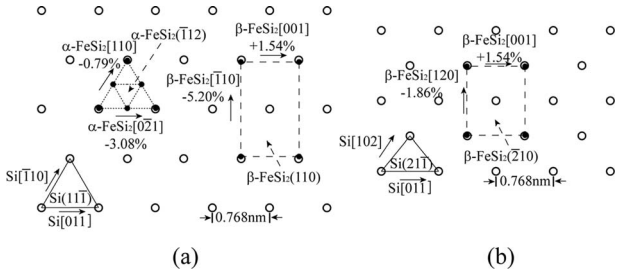

FIG. 10. Two-dimensional real space model between $FeSi_2$ (closed circles) and Si (open circles) matrix. (a) Both $(\bar{1}12)_\alpha$ and $(110)_\beta$ planes have an interface with $(11\bar{1})_{Si}$ planes and (b) the $(\bar{2}10)$ plane of β-$FeSi_2$ is faced with the $(21\bar{1})_{Si}$ plane with small linear mismatches.

of Fig. 8(b). In this figure, the interface between β-$FeSi_2$ and Si is indicated by a solid line. Also, the schematic diagrams of the corresponding atomic rows are shown in Fig. 9(b). It is apparent that misfit dislocations exist at the interface and their spacing is consistent with the distance of the strain contrasts in Fig. 8(a). However, it was difficult to find clear interface plane where the large-spacing contrasts were shown.

We succeeded in synthesizing small-sized β-$FeSi_2$ nanoparticles in the present study, but their amount was very small. We have recently found that the amount of β-$FeSi_2$ nanoparticles can be enhanced by optimizing the growth conditions. More extensive studies are currently underway, and the details will be reported elsewhere.

Finally, we discuss the factor to determine the morphology of nanoparticles. From the crystallographic point of view, cubic γ-$FeSi_2$ and Si can form the interface with a very low lattice mismatch because of their similarity in atomic arrangements at the interface. On the other hand, the crystallographic structures of tetragonal α- and orthorhombic β-$FeSi_2$ phases are quite different from that of Si, and therefore the deposited Fe atoms have a tendency to form nanoparticles by making an interface with low mismatching value. To analyze the relationship between morphology and interface energy, we calculated the linear mismatches from the two-dimensional real space model at the perpendicular direction of the interfaces. From the results of SAED, NBED, and FFT pattern analyses, we could know that basically most nanoparticles have an interface along $\{111\}_{Si}$ [angled hemisphere: $(\bar{1}12)_\alpha \| (11\bar{1})_{Si}$, asymmetric triangle: $(220)_\beta \| (1\bar{1}1)_{Si}$, hemispherical: $(1\bar{1}1)_\gamma \| (11\bar{1})_{Si}$, and columnar: $(1\bar{1}1)_\gamma \| (1\bar{1}1)_{Si}$ or $(\bar{1}11)_\gamma \| (11\bar{1})_{Si}$]. Figure 10(a) also shows the lattice plane configurations of epitaxially grown α- and β-$FeSi_2$ on Si (111) plane, and the linear mismatches of the $(\bar{1}12)_\alpha$ and $(110)_\beta$ on the $(11\bar{1})_{Si}$ correspond to the small values of −0.79% and −3.08% for α-$FeSi_2$ and +1.54% and −5.20% for β-$FeSi_2$. However, the interface plane of the nanoparticle formed in Si matrix is more complicated than that of the particle formed on Si substrate, because it is feasible to form different interface plane by diffusing Fe atom into Si matrix. In the case of β-$FeSi_2$, another possible heteroepitaxial relationship $[(\bar{2}10)_\beta \| (21\bar{1})_{Si}]$ exists as observed in Fig. 10(b). Figure 10(b) illustrates the lattice plane of $(21\bar{1})_{Si}$ and $(\bar{2}10)_\beta$ at the perpendicular direction to the inter-

face of Fig. 9(a). As the linear mismatches of this epitaxial relationship are smaller than those of $(110)_\beta$ on the $(11\bar{1})_{Si}$ [+1.54% and −1.86%], it is obvious that this interface can be preferentially formed during annealing process. Consequently, the shape of β-$FeSi_2$ nanoparticles becomes asymmetric triangle. It should be noted that the preferential interface planes between β-$FeSi_2$ and Si depend on the particle size. In fact, a β-$FeSi_2$/Si interface plane different from ours was observed in the large β-$FeSi_2$ nanoparticle.[35] This suggests that the strain state of β-$FeSi_2$ can be controlled by adjusting the particle size.

IV. CONCLUSIONS

We fabricated $FeSi_2$ nanoparticles on a Si(100) substrate and characterized their microstructures using TEM. The following results were obtained.

(1) Well-isolated nanoparticles with an average size of ~10 nm were successfully formed by an electron-beam evaporation of Fe onto a single crystal Si(100) substrate in combination with thermal annealing. Cross-sectional TEM observations revealed that deposited Fe particles diffuse into Si substrate and $FeSi_2$ nanoparticles with various morphologies are formed just beneath the substrate surface. These nanoparticles consisted of α-, β-, and γ-$FeSi_2$ phases and possessed epitaxial relationships with the Si substrate.

(2) Among the metastable phases, there are two types of γ-$FeSi_2$ phase: one is a hemispherical nanoparticle and the other is a columnar-shaped nanoparticle which shows moiré fringe images due to the overlapping of γ-$FeSi_2$ and Si lattices. On the other hand, α-$FeSi_2$ nanoparticles possess angled hemispherical shape due to the dissimilarity of structure between α-$FeSi_2$ and Si.

(3) Besides the above metastable phases, a small amount of β-$FeSi_2$ nanoparticles was formed. Unlike α- and γ-$FeSi_2$ phases, strain contrasts due to the lattice mismatch were observed at the interface between the β-$FeSi_2$ nanoparticle and Si substrate.

(4) The morphologies classified by the orientation relationships between the $FeSi_2$ nanoparticles and Si substrate are as follows.

(i) α-$FeSi_2$: $(\bar{1}12)_\alpha \| (11\bar{1})_{Si}$ and $[0\bar{2}1]_\alpha \| [011]_{Si}$, angled hemisphere;

(ii) β-$FeSi_2$: $(220)_\beta \| (1\bar{1}1)_{Si}$ and $[001]_\beta \| [011]_{Si}$, asymmetric triangle;

(iii) γ-$FeSi_2$: $(004)_\gamma \| (400)_{Si}$ and $[110]_\gamma \| [011]_{Si}$ hemispherical; and

(iv) $(1\bar{1}1)_\gamma \| (1\bar{1}1)_{Si}$ or $(\bar{1}11)_\gamma \| (11\bar{1})_{Si}$ and $[110]_\gamma \| [011]_{Si}$, columnar.

(5) It is obvious that the morphologies of nanoparticles are determined by the lattice mismatch between nanoparticle and Si substrate. It was found that the β-$FeSi_2$ nanoparticle in Si matrix is sufficiently small (several nanometers); β-$FeSi_2$ nanoparticle is inclined to form the interface plane with epitaxial relationship of $(\bar{2}10)_\beta \| (21\bar{1})_{Si}$.

ACKNOWLEDGMENTS

This research was partially supported by the 21st Century Center of Excellence program "Towards Creating New Industrials Based on Inter-Nanoscience" from the Ministry of Education, Culture, Sport, Science and Technology, Japan. One of the authors (M.I.) also acknowledges the financial support from the Hosokawa Powder Technology Foundation.

[1] O. Kubaschewski, *Iron-Binary Phase Diagrams* (Springer, Berlin, 1982).
[2] M. C. Bost and J. E. Mahan, J. Appl. Phys. **58**, 2696 (1985).
[3] N. E. Christensen, Phys. Rev. B **42**, 7148 (1990).
[4] S. J. Clark, H. M. Al-Allak, S. Brand, and R. A. Abram, Phys. Rev. B **58**, 10389 (1998).
[5] K. Lefki and P. Muret, J. Appl. Phys. **74**, 1138 (1993).
[6] M. Takeda, M. Kuramitsu, and M. Yoshio, Thin Solid Films **461**, 179 (2004).
[7] A. Rizzi, B. N. E. Rössen, D. Freundt, Ch. Dieker, and H. Lüth, Phys. Rev. B **51**, 17780 (1995).
[8] J. E. Mahan, V. L. Thanh, J. Chevrier, I. Berberzier, J. Derrien, and R. G. Long, J. Appl. Phys. **74**, 1747 (1993).
[9] D. Leong, M. Harry, K. J. Reeson, and K. P. Homewood, Nature (London) **387**, 686 (1997).
[10] Z. Liu *et al.*, Sol. Energy Mater. Sol. Cells **90**, 276 (2006).
[11] M. Tanaka, Y. Kumagai, T. Suemasu, and F. Hasegawa, Appl. Surf. Sci. **117/118**, 303 (1997).
[12] M. Han, M. Tanaka, M. Takeguchi, Q. Zhang, and K. Furuya, J. Cryst. Growth **255**, 93 (2003).
[13] N. Onda, J. Henz, E. Muller, K. A. Mader, and H. von Kanel, Appl. Surf. Sci. **56–58**, 421 (1992).
[14] J. Chevier, V. Le Thanh, S. Nitsche, and J. Derrien, Appl. Surf. Sci. **56–58**, 438 (1992).
[15] L. T. Vinh, J. Chevrier, and J. Derrien, Phys. Rev. B **46**, 15946 (1992).
[16] Z. Yang, K. P. Homewood, M. S. Finney, M. A. Harry, and K. J. Reeson, J. Appl. Phys. **78**, 1958 (1995).
[17] T. Suemasu, Y. Negishi, K. Takakura, F. Hasegawa, and T. Chikyow, Appl. Phys. Lett. **79**, 1804 (2001).
[18] M. A. Lourenco, R. M. Gwilliam, G. Shao, and K. P. Homewood, Nucl. Instrum. Methods Phys. Res. B **206**, 436 (2003).
[19] D. B. Migas and L. Miglio, Phys. Rev. B **62**, 11063 (2000).
[20] Q. Zhang, M. Tanaka, M. Takeguchi, M. Han, and K. Furuya Jpn. J. Appl. Phys., Part 1 **42**, 4667 (2003).
[21] Y. Ozawa, T. Ohtsuka, C. Li, T. Suemasu, and F. Hasegawa, J. Appl. Phys. **95**, 5483 (2004).
[22] A. Wohllebe, B. Holländer, S. Mesters, C. Dieker, G. Crecelius, W. Michelsen, and S. Mantl, Thin Solid Films **287**, 93 (1996).
[23] B. Bian, K. Sato, and Y. Hirotsu, Appl. Phys. Lett. **75**, 3686 (1999).
[24] K. Sato and Y. Hirotsu, J. Appl. Phys. **93**, 6291 (2003).
[25] K. Sato, Y. Hirotsu, H. Mori, Z. Wang, and T. Hirayama, J. Appl. Phys. **98**, 024308 (2005).
[26] E. R. Weber, Appl. Phys. A: Solids Surf. **30**, 1 (1983).
[27] C. G. Granqvist and R. A. Buhrman, J. Appl. Phys. **47**, 2200 (1976).
[28] X. W. Lin, M. Behar, J. Desimoni, H. Bernas, J. Washburn, and Z. Liliental-Weber, Appl. Phys. Lett. **63**, 105 (1993).
[29] Z. Yang, G. Shao, and K. P. Homewood, Appl. Phys. Lett. **68**, 1784 (1996).
[30] M. Behar, H. Bernas, J. Desimoni, X. W. Lin, and R. L. Maltez, J. Appl. Phys. **79**, 752 (1996).
[31] J. Desimoni, H. Bernas, M. Behar, X. W. Lin, J. Washburn, and Z. Liliental-Weber, Appl. Phys. Lett. **62**, 306 (1993).
[32] G. Shao and K. P. Homewood, Intermetallics **8**, 1405 (2000).
[33] E. J. Kirkland, *Advanced Computing in Electron Microscopy* (Plenum, New York, 1998).
[34] M. De Graef, *Introduction to Conventional Transmission Electron Microscopy* (Cambridge University Press, Cambridge, 2003).
[35] M. Itakura, D. Norizumi, T. Ohta, Y. Tomokiyo, and N. Kuwano, Thin Solid Films **461**, 120 (2004).